

Ultra-Wideband Localization: Advancements in Device and System Calibration for Enhanced Accuracy and Flexibility

Risang Yudanto , Jianqiao Cheng , Erik Hostens , Miel Van der Wilt , and Mats Vande Cavey 

Abstract—We show how the state of use of ultra-wideband (UWB) system is improved by removing systematic errors (bias) on device-level to improve accuracy and apply simple procedure to automate calibration process on the system-level to reduce manual efforts. On device-level, we discern the different sources of bias and establish a method that determines their values, for specific hardware and for individual devices. Our comprehensive approach includes simple, easy-to-implement methodologies for compensating these biases, resulting in a significant improvement in ranging accuracy. The mean ranging error has been reduced from 0.15 to 0.007 m, and the three-sigma error margin has decreased from 0.277 to approximately 0.103 m. To demonstrate this, a dedicated test setup was built. On system-level, we developed a method that avoids measuring all anchor positions one by one by exploiting increased redundancy from anchor-to-anchor and anchor-to-tag ranges, and automatically calculating the anchors topology (relative positions between each other). Nonlinear least squares provides the maximum likelihood estimate of the anchor positions and their uncertainty. This approach not only refines the accuracy of tag localization but also offers a predictive measure of its uncertainty, giving users a clearer understanding of the system's capabilities in real-world scenarios. This system-level enhancement is further complemented by the integration of a ranging protocol called automatic UWB ranging any-to-any, which offers additional layers of flexibility, reliability, and ease of deployment to the UWB localization process.

Index Terms—Clock frequency compensation, maximum likelihood estimation (MLE), nonlinear squares (NLS), real-time location systems (RTLS), topology discovery (TD), ultra-wideband (UWB) calibration, UWB localization, UWB protocol.

I. INTRODUCTION

POSITIONING technologies can be classified into two primary domains: outdoor and indoor applications. While the global positioning system (GPS) effectively addresses outdoor contexts, the indoor positioning systems, particularly real-time location systems (RTLS), still pose intricate challenges that capturing heightened attention from the scientific and business communities [1]. The RTLS enable user to digitally track the real-time location and movements of physical things throughout large indoor facilities, providing a real-time visualization of the locations of essential personnel, vital assets, and key equipment [2]. In addition, this data can be seamlessly incorporated into automated processes, including Internet-of-Things (IoT)-driven safety measures and asset and supply chain management systems. Essentially, RTLS unlock the same location-aware value that GPS has created in outdoor scenarios for indoor spaces where GPS is unavailable. It serves as cornerstone of digital

innovation, IoT, Industry 4.0, and digital twin technology [3], [4]. It is also helping organizations in healthcare, manufacturing, warehouses, etc., by improving safety, boosting efficiency, and driving business results [5].

The landscape of indoor RTLS technologies vary from building-independent systems, such as image-based technologies and dead reckoning, to building-dependent solutions employing radio frequency (RF) technologies [6]. An extensive review of building-independent systems can be find in [2]. As for RF-based methods, early solutions, such as infrared and Bluetooth, excelled in confined areas but degrades in larger areas due to potential interference in multipath settings [7]. Wi-Fi leveraged existing infrastructure for location services but sometimes traded off accuracy [5]. Radio frequency identification excels in item-level tracking, especially for warehouses, yet struggles in environments rich in metal or liquid and needs closer proximity for accurate readings [8]. Visible light and ultrasonic solutions offer accuracy in controlled settings but depend on a direct line-of-sight (LoS), limiting their versatility [9]. 5G-based localization, evolving with each new 3GPP release, promises high accuracy and wide coverage for future RTLS. However, its full potential and scalability remain to be thoroughly assessed [10]. Hybrid systems that combine multiple technologies are gaining attention for their ability to mitigate individual limitations, and a detailed discussion is available in [11]. Within this diverse landscape, ultra-wideband (UWB) stands out with its high adaptability, offering centimeter-level precision, low-power consumption, and robustness to RF interference and multipath effects [12].

Manuscript received 3 November 2023; revised 29 November 2023; accepted 2 December 2023. Date of publication 5 December 2023; date of current version 28 December 2023. This work was supported in part by the Flanders Innovation and Entrepreneurship (VLAIO) carried out within the framework of Flanders Make's ICON project UWB_Autoconfig (Autoconfiguration for UWB localization and communication, HBC.2020.2010) and in part by Flanders Make. (Corresponding author: Risang Yudanto.)

The authors are with Flanders Make, 3001 Heverlee, Belgium (e-mail: risanggotot.yudanto@flandersmake.be; jianqiao.cheng@flandersmake.be; erik.hostens@flandersmake.be; miel.vanderwilt@flandersmake.be; mats.vandecavey@flandersmake.be).

Digital Object Identifier 10.1109/JISPIN.2023.3339602

While UWB exhibits remarkable capabilities, certain challenges remain to be addressed. The first challenge is its accuracy, while noteworthy, can be disrupted by systematic errors. While random errors can be corrected for by suitable filtering techniques [13], including exploiting position correlations over time [14], [15], the accuracy and robustness of UWB localization are mainly hampered by these *systematic* errors. These errors, whether intrinsic to the hardware or induced by the environment, consistently appear during measurements [16]. For the mitigation of these systematic errors, they have to be explicitly determined through dedicated experiments, or inferred from the redundancy in a measurement campaign involving many devices, prior to the UWB localization itself. In addition, UWB's setup and calibration require meticulous attention, demanding specialized expertise to ensure system reliability. In dynamic environments, preserving UWB's accuracy can be resource-intensive and necessitates continuous oversight.

Contributions: Building upon these challenges, the primary contributions of this article are summarized as follows.

- 1) We address device biases from hardware directly through comprehensive calibration methodologies with experimental validations. Different from deep learning approaches [14], our solutions do not require extensive training phases and can be implemented easily in embedded electronics. This work specifically targets anomalies including the following.
 - a) *Clock frequency offsets (CFO)*: We present two distinct methods: one utilizes a reference clock for frequency offset calibration, the other operates independently and does not need a reference clock.
 - b) *Received signal strength (RSS)*: An empirical model is formulated to simulate the biases introduced by different RSS. An approach to compensate these biases is also provided.
 - c) *Hardware delay*: We introduce a straightforward technique that leverages a single distance measurement for hardware delay calibration.
- 2) We introduce a novel method for fast and flexible anchor coordinates measurement that demands little manual intervention. Importantly, our approach also offers an uncertainty assessment concerning anchor displacement, guiding strategies, such as placing more anchors or enhancing anchor localization.
- 3) We designed a protocol that optimizes UWB device communication and prevents potential conflicts. Besides supporting our anchor measurement methodology, it also facilitates novel applications include simultaneous localization and calibration (SLAC), clock calibration without a reference clock, and localization using downlink Time Difference of Arrival (DL-TDoA). We provide detailed guidelines for these implementations.
- 4) All proposed systems and methodologies have been implemented and tested using real UWB ranging data from off-the-shelf hardware.

The rest of this article is organized as follows. Section II elucidates typical elements that contribute to systematic errors in UWB ranges and provides detailed corrective measures.

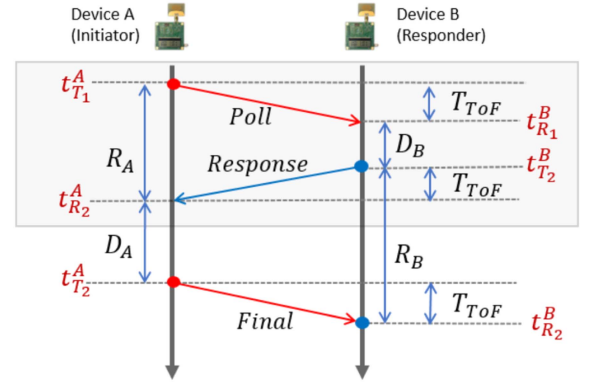


Fig. 1. ToF measurement using TWR, with SS-TWR Protocol (shaded) and DS-TWR Protocol. Timestamp is generated every time UWB signal leaving the transmitter ($t_{T_n}^A, t_{T_n}^B$) or detected at receiver ($t_{R_n}^A, t_{R_n}^B$). From these timestamps, a ToF can be calculated.

Section III introduces a novel system calibration methodology aimed at automating the estimation of 3-D world coordinates for a device in UWB RTLS. Section IV delves into our custom UWB communication protocol, AURA, explaining its support for system calibration and its adaptability to advanced applications, such as SLAC and DL-TDoA. Both device calibration and system calibration can be applied independently, as each aims to enhance UWB performance from distinct perspectives. AURA, as a benchmark protocol, is beneficial to understand but not a prerequisite for grasping the concepts in the other sections.

II. DEVICE CALIBRATION

In this section, we investigate various sources of errors from intrinsic hardware characteristics that contribute to systematic errors, with a particular emphasis on: CFO, RSS, and hardware delay [17]. This section also provides a comprehensive guide for a step-by-step device calibration process aimed at mitigating these errors. We use different evaluation boards in combination with different antennas as experimental platforms to gather data and validate the method by using them for distance estimation. Although the different boards used in our experiments are based on DW1000 chipset, we emphasize that our method is agnostic to UWB system manufacturer brands. For distance estimation, UWB systems typically employ single-sided two-way ranging (SS-TWR) or double-sided two-way ranging (DS-TWR) techniques [18], leveraging timestamped message exchanges between transceivers to calculate time-of-flight (ToF). The standard protocol for SS-TWR and DS-TWR is depicted in Fig. 1, where the initiator A starts the TWR process by sending a *Poll* message. Upon receiving the packet, responder B sends a *Response* packet back to initiator A after some response delay time D_B . Initiator device A then receives the response packet and measure the round-trip time (RTT) R_A . At this point, a ToF can already be computed using SS-TWR

$$T_{\text{ToF}} = \frac{1}{2} (R_A - D_B). \quad (1)$$

As for DS-TWR, a *Final* message can be sent by initiator A indicating the end of TWR process and enable calculation of

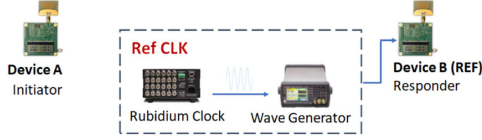


Fig. 2. Setup for absolute clock calibration, with reference clock feeding one of the transceiver.

ToF using [19]

$$T_{\text{ToF}} = \frac{(R_A \cdot R_B) - (D_A \cdot D_B)}{R_A + D_A + R_B + D_B}. \quad (2)$$

A. CFO Calibration

Real-world applications face complications from non-identical clock frequencies in transmitters (Tx) and receivers, due to factors, such as manufacturing tolerances, temperature fluctuations, and random frequency drifts [20]. This CFO subsequently introduces time errors into the derived ToF. Although DS-TWR inherently displays resistance to CFO [21], SS-TWR experiences significant degradation in ranging accuracy. This section aims to provide two distinct methods to calibrate CFO that enables SS-TWR to achieve the same accuracy levels comparable to DS-TWR.

Referring to Fig. 1, by denoting the CFO introduced by devices A and B as ϵ_A and ϵ_B , respectively, in parts per million (ppm), we formulate the ToF error in SS-TWR using the methodology in [22] as

$$\epsilon_{\text{ToF}} = T_{\text{ToF}} \cdot \epsilon_A + \frac{1}{2} D_B \cdot (\epsilon_A - \epsilon_B). \quad (3)$$

Conventionally, it is assumed that $T_{\text{ToF}} \ll D_B$ since the reply time D_B is on the order of milliseconds, whereas T_{ToF} is typically on the order of nanoseconds. Similarly, according to [22], ToF error of DS-TWR is formulated as

$$\epsilon_{\text{ToF}} = \frac{1}{2} T_{\text{ToF}} \cdot (\epsilon_A + \epsilon_B). \quad (4)$$

This explains the limited impact of CFO errors in DS-TWR.

Under ideal conditions, when devices exhibit no CFO (i.e., $\epsilon_A = \epsilon_B = 0$), the time interval between *Poll* and *Final* messages should be equal at A and B, or $(t_{T_2}^A - t_{T_1}^A) = (t_{R_2}^B - t_{R_1}^B)$, or $R_A + D_A = D_B + R_B$. These values can be measured from the devices, allowing us to leverage this concept for calibration purposes. In the following, we present two calibration methods: absolute clock calibration and relative clock calibration.

Absolute clock calibration: The first approach involves performing CFO measurements on all utilized UWB transceiver devices against a reference clock. The experimental setup is depicted in Fig. 2. We use a waveform generator, that generates the nominal 38.4 MHz clock signal as required by the DW1000 chip, as the source clock to the reference device, which is the device B in this setup. The signal generator uses Rubidium frequency standard FS725 that gives a stable 10 MHz sine signal as the input reference clock. After executing the TWR, we measure $R_A + D_A$ and $R_B + D_B$. By doing so, device B can correlate its own clock with device A's clock by calculating the clock factor f_{AB} (i.e., the frequency ratio between clock A

and clock B) using

$$f_{AB} = \frac{(t_{T_2}^A - t_{T_1}^A)}{(t_{R_2}^B - t_{R_1}^B)} = \frac{R_A + D_A}{R_B + D_B}. \quad (5)$$

Since the time measurement from device B is considered accurate, we calculate the clock offset of device A in ppm using

$$\epsilon_A = 10^6 \cdot (f_{AB} - 1). \quad (6)$$

The frequency offset ϵ_A against reference clock for each device is measured after the device has reached steady state (after sufficient warm-up time) and at room temperature around 25 °C. The value ϵ_A can be stored in a calibration database or in each device's memory and then used to correct every measured UWB timestamp. Given that this method relies on an accurate reference clock, which is typically bulky in volume, it is commonly performed upfront in a one-off calibration process. However, it should be noted that the CFO of a crystal oscillator may exhibit drift over time. Consequently, when conducting measurements at different times and/or locations, it is possible for the actual frequency offset to have changed, and the calibration value from the database or device's memory might not be accurate anymore.

Relative clock calibration: The second approach requires the system to perform the following operations. After the first round of TWR communication, the responder (device B) obtains information about device A (i.e., R_A , D_A measured by A's clock) and inherently has knowledge about itself (i.e., D_B , R_B measured by B's clock). Consequently, the clock factor f_{AB} can be calculated following (5). In this case, the reply delay D_B at device B can be computed using device A's clock, i.e., $D_B \cdot f_{AB}$. Since everything can be calculated in A's clock reference, only ϵ_A will have influence on the error and (3) becomes

$$\epsilon_{\text{ToF}} = \frac{1}{2} (R_A - D_B \cdot f_{AB}) \cdot \epsilon_A = T_{\text{ToF}} \cdot \epsilon_A. \quad (7)$$

Hence, the error introduced by CFO is not influenced anymore by the response delay D_B and becomes only a function of ToF, which is very small compared to D_B .

In our TWR protocol, the measured reply delay D_B and computed clock factor f_{AB} are shared by device B (responder) in every *Response* message, while the measured relative timestamps at device A (R_A and D_A) are shared by device A (initiator) in every *Final* message. In this way the clock-corrected SS-TWR can be immediately computed at both initiator and responder side.

Relative clock calibration offers several notable advantages due to its flexibility and cost-effectiveness. Unlike absolute clock calibration methods that often require expensive and bulky equipment, the relative clock calibration method proves to be more accessible and economical. This characteristic makes it particularly suitable for online implementation. Furthermore, the use of relative clock calibration enhances the system's robustness against frequency drift over time. By continuously measuring and updating the clock factor during each TWR process, the calibration remains adaptive and accounts for any variations in clock frequency.

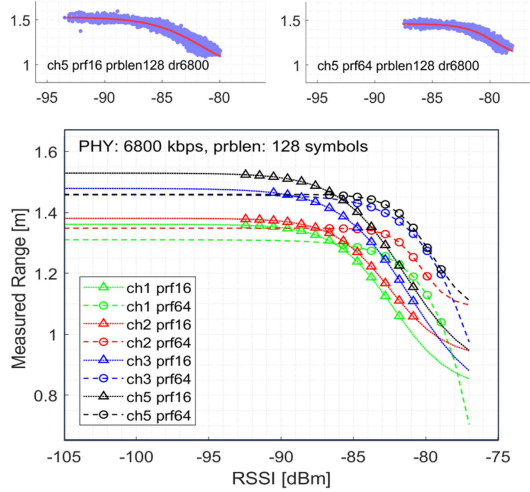


Fig. 3. Top: UWB range measurements [m] versus RSSI [dBm] from some of the testsets with combinations of UWB settings at Channel 5, PHY 6800 kbps and 128 symbols preamble, with PRF 16 MHz (left) and PRF 64 MHz (right). The red line in each graph represents the fitted tanh model to the measurement. Bottom: all fitted tanh models for PHY 6800 kbps, 128 symbols preamble for different channels and PRF.

B. RSS Calibration

The second factor impacting the ranging performance of the Decawave system is the RSS, as the accuracy of the received timestamp deteriorates when the received power of the direct path signal increases [23].

To establish the relationship between received power and bias error, we conducted a series of experiments, in which we applied systematic changes in the power level while maintaining a constant true distance between the UWB devices. The setup is very similar as the one in Fig. 2, except that the antennas on both transceivers are replaced with 1-m RF cables. This modification was implemented to eliminate any potential effects arising from wireless channels and antenna orientations, by ensuring that the actual distances remained consistent throughout the tests.

In our comprehensive study, we systematically adjust the transmit power gain from 0 to 18 dB in steps of 0.5 dB. For each level, a collection of at least 1000 TWR samples is assembled. Within each sample, we record all the important data from the TWR measurement including the relative timestamps (R_A , D_A , R_B , and D_B from Fig. 1), signal diagnostics and channel impulse responses. We then employ the DS-TWR protocol to estimate the distance and compute received signal strength indicator (RSSI) and first path power level following guidelines in the DW1000 manual [24]. The data collection is conducted under different UWB configurations supported by the DW1000: PHY data rates (110, 850, and 6800 kbps), frequency channels (1, 2, 3, 4, 5, and 7), pulse repetition frequency (PRF) (16 and 64 MHz) and preamble lengths (64, 128, 256, 512, 1024, 2048, and 4096 symbols). The process is then repeated for different UWB devices hosting the same chip.

Ideally, the measured ranges in these experiments should be constant regardless of the received power level. Contrary to this expectation, Fig. 3 reveals varying ranges corresponding to different received power. The relation between RSSI and bias is

also not exactly the same for different UWB settings, though they show the same trend in which the bias versus RSSI is more linear at lower RSSI (e.g., at $\text{RSSI} < -84\text{ dBm}$ for PRF 64 MHz or $\text{RSSI} < -86\text{ dBm}$ for PRF 16 MHz). Measured ranges typically exceed 1 m due to the slower light speed in the RF cable between transceivers compared to free space.

We have evaluated various models for fitting the RSSI-to-bias relation, including high-order polynomial functions, support vector regression, and a tanh model [25]. Results revealed that the tanh model consistently yields good results. It is also quite easy to be implemented on embedded platforms. The tanh model is expressed as

$$\text{bias}(\text{RSSI}) = a_1 \tanh(a_2(\text{RSSI} + a_3)) + a_4 \quad (8)$$

where model coefficients $a_1 \dots a_4$ are fitted to the data. In our observations, a_1 , a_2 , and a_3 are very similar for different UWB devices operating with the same configuration settings. They also do not change a lot in different environmental conditions. The model coefficients a_1 , a_2 , and a_3 for different UWB settings are then stored in the calibration database. The last coefficient a_4 , which determines a global bias shift, is determined by the hardware delay calibration. It is device-specific, therefore it is usually different for different devices.

C. Hardware Delay Calibration

Hardware delay typically refers to the signal travel time within a device and is predominantly influenced by the material and length of the track between antenna and the chip's RF front end. After warming up, these delays typically remain constant for each device, enabling their estimation before initiating ranging procedures [16].

In the transmission process, consider t_{T_1} as the actual moment the signal departs from the transmitting antenna, while \hat{t}_{T_1} denotes the timestamp registered within the transmitter chip. Consequently, the hardware delay X_T represents the lag between actual transmission and the system-recorded time, defined as $X_T = t_{T_1} - \hat{t}_{T_1}$. Similarly, during the reception process, the true time when a signal is received at the antenna is t_{R_1} , and the timestamp recorded by the chip is \hat{t}_{R_1} . The delay in the receiver is $X_R = \hat{t}_{R_1} - t_{R_1}$. Therefore, the aggregate time error attributed to hardware delay within a single signal transmission and reception cycle for this device is given by $X = X_T + X_R$.

Referring to Fig. 1 and taking into consideration the hardware delay, the RTT R_A can be computed from the equation

$$\begin{aligned} &(\hat{t}_{R_2}^A - X_{A_R}) - (\hat{t}_{T_1}^A + X_{A_T}) \\ &= (\hat{t}_{R_2}^A - \hat{t}_{T_1}^A) - (X_{A_R} + X_{A_T}) \end{aligned} \quad (9)$$

and similarly for the response delay D_B , which can be extracted from

$$\begin{aligned} &(\hat{t}_{T_2}^B + X_{B_T}) - (\hat{t}_{R_1}^B - X_{B_R}) \\ &= (\hat{t}_{T_2}^B - \hat{t}_{R_1}^B) + (X_{B_T} + X_{B_R}). \end{aligned} \quad (10)$$

In summary: $R_A = \hat{R}_A - X_A$ and $D_B = \hat{D}_B + X_B$, with $X_A = X_{A_T} + X_{A_R}$ and $X_B = X_{B_T} + X_{B_R}$. By substituting the definitions of R_A and D_B , we can deduce that the time error

caused by hardware delay in SS-TWR is

$$\epsilon_{\text{HW}_{\text{SS}}} = \frac{1}{2} (X_A + X_B). \quad (11)$$

Following the calculation in [22], we can determine the time error due to hardware delay in DS-TWR as

$$\epsilon_{\text{HW}_{\text{DS}}} = \frac{(\hat{R}_B + \hat{D}_B) X_A + (\hat{R}_A + \hat{D}_A) X_B}{\hat{R}_A + \hat{R}_B + \hat{D}_A + \hat{D}_B}. \quad (12)$$

Hence, as long as the values of X_A and X_B are known, the time error attributable to hardware delay can be calculated.

To estimate the values of X in real-world scenarios, we have developed a simple calibration method requiring just a single distance measurement. This approach uses the RSSI-to-bias model explained in Section II-B and requires a minimum of three reference devices A, B, and C, with identical RF circuits, Tx power levels, and antenna configurations. The hardware delay estimation process can be summarized as follows.

- 1) Position devices A and B at a distance where the RSSI is sufficiently low to ensure the bias (RSSI) lies within the linear regime (e.g., at RSSI < -84 dBm for PRF 64 MHz or RSSI < -86 dBm for PRF 16 MHz); ensure a clean, LoS communication channel; maintaining consistent relative orientations to avoid extra bias due to varying antenna orientations.
- 2) Perform UWB DS-TWR measurements: A as initiator, B as responder, and vice versa; measure ground truth with a laser meter. Alternatively, SS-TWR can also be used but the clock should then be calibrated.
- 3) Iterate the process for different device pairings: A-C, B-C, ...

By obtaining a minimum of three equations with three unknown delays (X_A , X_B , and X_C), hardware delay offsets can be effectively computed. Additional devices requiring calibration can either adopt the procedure above and calculate hardware delay using least squares methods, or use a previously calibrated device as a reference to determine hardware delay on the uncalibrated device. Thus, this method can be extended to any number of devices.

D. Experimental Validation

For validation of the device calibration, we measure the TWR between two UWB devices-under-test (DUT) at a time, one mounted on a pole on a fixed platform and the other on a pole on a moving platform on a linear slider, see Fig. 4. Different scenarios are applied including: transmit at different power levels, different hardware boards and antennas (MDEK1001 with integrated antenna, TREK1000 with external antennas: original antenna, Taoglas FXUWB10, and Taoglas TU.60.3H31), combining linear and rotary movement, etc.

Fig. 5 presents one of our validation experiments. In this setup, two DUTs were engaged and they alternated roles between initiator and responder with each TWR cycle. The figure elucidates three key metrics: the raw measured distance between the DUTs, the range errors prior to any calibration, and the refined errors

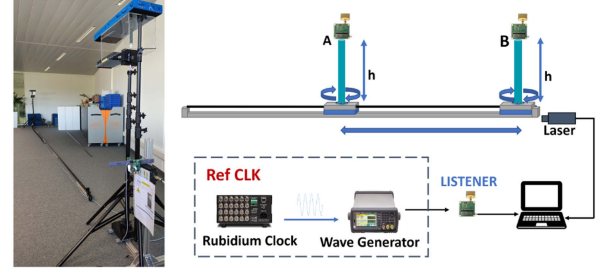


Fig. 4. Validation setup where the DUT are mounted on the poles. One pole can move in linear direction and the displacement is continuously measured by the laser. Both poles can rotate and are adjustable in height. A listener connected to reference clock captures all data and forward them to the PC for analysis.

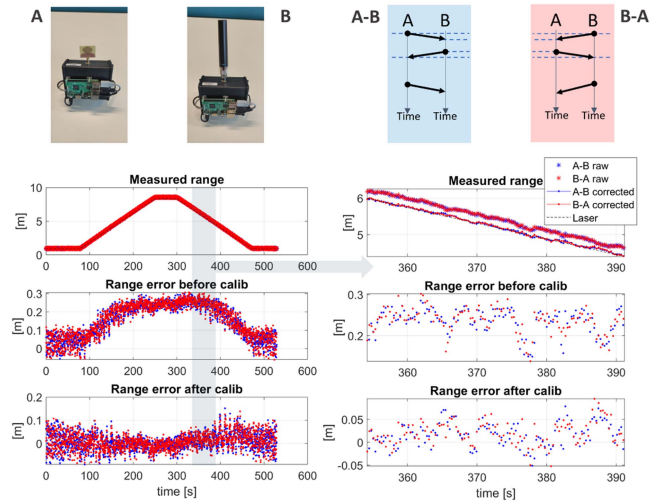


Fig. 5. One of the validations using TREK1000 boards with original antenna (DUT A) and Taoglas TU.60.3H31 (DUT B) (pictures on top left). DUT A moves on linear slide and continuously rotating, while DUT B is static. They transmit at different Tx power levels. Both DUTs are alternating the roles of initiator and responder after each TWR cycle (top right scheme). The graphs show the measured distance (top), range error before applying device calibration (middle), and after applying device calibration (bottom). The right side is the zoom of the left graphs on the section highlighted by the shadow.

post our device calibration. This calibration process primarily mitigates errors from CFO, RSSI, and hardware delay.

To further evaluate the accuracy enhancement achieved through our device calibration, we present comprehensive statistical results in Fig. 6. It can be clearly seen from the figure that the application of device calibration leads to a significant improvement in accuracy. In addition, while CFO effects are more prominent in SS-TWR, they are less noticeable in DS-TWR. The histograms and cumulative distribution function (CDF) graphs confirm the similar performance of fully calibrated SS-TWR and DS-TWR.

III. SYSTEM CALIBRATION

As previously discussed, ToF calculations in a TWR measurement require at least one initiator and one responder, determined either through SS-TWR or DS-TWR methods. Within

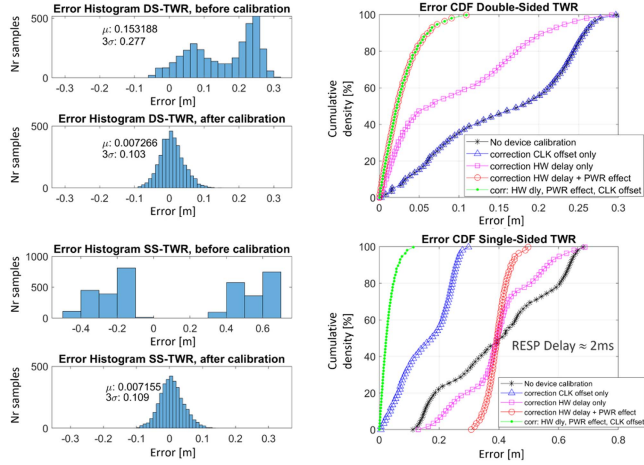


Fig. 6. Statistical results before and after device calibration from experiments reported in Fig. 5 for both DS-TWR (top) and SS-TWR (bottom). The enhanced accuracy post-calibration is evident. Notably, CFO effects are more pronounced in SS-TWR than in DS-TWR. Histograms and CDF graphs reveal comparable performance between fully calibrated SS-TWR and DS-TWR.

UWB localization systems, mobile devices are typically labeled as tags, while stationary ones are referred to as anchors. Depending on the applications, tags might serve as initiators with anchors responding, or vice versa. Conventionally, these roles remain fixed, where measurements or rangings take place between initiators (tags) and responders (anchors), and there is no interaction between either initiators themselves or responders themselves unless manually adjusted. Such a system is suitable for environments where anchor positions are static and their world coordinates are predetermined with an accuracy up to centimeter level.

A. Problem Statement

In practical situations the implementation of determining accurate anchor coordinates presents significant challenges. The task typically demands the cumbersome manual measuring of each separate anchor's position, often involving the use of specialized surveying instruments, such as the total station. The amount of required labor is dominant especially in large-scale applications, such as inventory management or warehouse monitoring, where the space is vast and the number of anchors considerable. Similarly, in temporary setups, such as geofencing for events or live demonstrations, there is an urgent need for rapid deployment. Furthermore, there are applications that do not require the absolute positioning of devices in world coordinates, but relative positioning suffices. Here, the inherent rigidity of the traditional model reveals its limitations, especially when anchors are integrated onto mobile platforms, such as drones or robots. This underscores a pressing demand for a system that is adaptable to both static and dynamic environments, and one that allows for quick and efficient acquisition of anchor coordinates and topology.

To address these challenges, we have delved into an innovative approach. This methodology not only simplifies the often tedious process of anchor localization but also introduces the possibility of dynamic configurations, making setups more

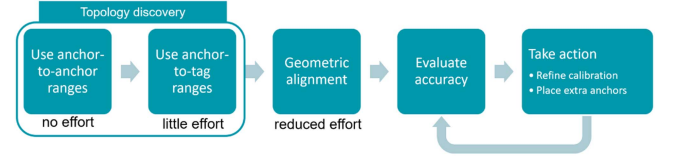


Fig. 7. Block diagram of system calibration procedure.

flexible and efficient. We have termed this complete procedure as “system calibration.” The detailed system calibration procedure of our approach is laid out as follows, complemented by a block diagram illustrated in Fig. 7.

- 1) *Use anchor-to-anchor (A2A) ranges*: By enabling the ranging process to incorporate not just interactions between anchors and tags, but also between the anchors themselves, we obtain more information about the system. This A2A ranging enables the discernment of the relative positions of anchors concerning one another, a procedure we have named “topology discovery” (TD).
- 2) *Use anchor-to-tag (A2T) ranges*: Since A2A ranges can be subject to biases, particularly in nonline-of-sight (NLOS) situations or due to local reflections (a common occurrence when anchors are placed close to metallic structures), we integrate the A2T ranging mechanism. This combination with A2A ranging significantly enhances the robustness and redundancy of the TD process.
- 3) *Topology discovery*: By combining A2A with A2T ranging, the entire anchor topology can be discerned efficiently and automatically, minimizing the need for manual effort.
- 4) *Geometric alignment (GA)*: With the topology now discovered, we derive the remaining spatial and rotary degrees-of-freedom of the entire system, by manually measuring a subset of merely four anchors.
- 5) *Evaluate accuracy*: To ascertain the accuracy of the system, a tag can be strategically placed or moved across various positions. By doing so, we can capture crucial range statistics, such as the localization uncertainty associated, with the current anchors or tags.
- 6) *Take action*: Finally, given the range statistics, we can make informed improvements/adjustments for the system, such as eliminating biased ranges or optimizing anchor placements. These actions are followed by a re-evaluation of the accuracy (see Step 5), possibly leading to an iterative procedure until the accuracy meets the requirements of the application.

It is essential to clarify that the automation aspect in this procedure refers predominantly to the TD, while the full system calibration itself is not fully automatic since some manual interventions are still required, for instance in the GA process. Despite this, our methodology leads to a significant reduction in manual calibration efforts. In this section, we explain how this is done in a statistically consistent way. The analysis is done for TWR, but is analogous for time difference of arrival (TDoA).

In addition, since the landscape of UWB systems continually evolves, and with the added intricacy presented by A2A ranging, there arises a significant need for a sophisticated yet intuitive

protocol. To meet this need, we have crafted the automatic UWB ranging any-to-any protocol (AURA). AURA has been meticulously designed not only to facilitate the TD phase of system calibration but also to foster seamless, conflict-free communication within advanced UWB frameworks. A detailed exploration of AURA can be found in Section IV.

B. Maximum Likelihood Estimate (MLE)

The most comprehensive representation of TD is the posterior probability distribution $p(x_i|r_{ij})$ of all device positions $x_i \in \mathbb{R}^3$ given all UWB ranges $r_{ij} \in \mathbb{R}$ between device positions x_i and x_j , if available. Assuming no prior information on the device positions, it follows using Bayes' rule that $p(x|r) \propto p(r|x)$. Upon inspection of UWB ranges compared with the true ranges after device calibration, it is reasonable, for LOS conditions, to assume a zero-mean normal distribution of the UWB range errors ϵ_{ij} , defined by

$$r_{ij} = \|x_i - x_j\| + \epsilon_{ij}, \text{ with } \epsilon_{ij} \sim \mathcal{N}(0, \sigma_{\text{UWB}}^2). \quad (13)$$

It is a well-known result that for normal errors the MLE is given by the nonlinear least squares (NLS) optimum \hat{x} of the cost function

$$\sum_{ij} \left(\frac{r_{ij} - \|\hat{x}_i - \hat{x}_j\|}{\sigma_{\text{UWB}}} \right)^2. \quad (14)$$

Using Laplace's method, the MLE covariance matrix $\text{Cov}[\hat{x} - x]$ is approximately the inverse of the NLS Hessian [26]. The covariance matrix related to only the anchors can be simply cropped out from the complete covariance matrix of all device positions by selecting the corresponding rows and columns. This derived covariance matrix can be used to evaluate the remaining uncertainty in the anchor positions estimate and as such to decide whether more measurements are needed. We will come back to this in Section III-E.

At this point, it is useful to decide, which UWB ranges should have been left out in the TD because of NLOS or reflections. Indeed, because of the increased redundancy, we can better statistically evaluate, which ϵ_{ij} do not meet the assumed zero-mean distribution, and are outliers. As we cannot directly evaluate the true ϵ_{ij} , we look at their estimates

$$\hat{\epsilon}_{ij} = r_{ij} - \|\hat{x}_i - \hat{x}_j\|. \quad (15)$$

The $\hat{\epsilon}_{ij}$ that fall outside $[-3\sigma_{\text{UWB}}, +3\sigma_{\text{UWB}}]$ are potential outliers and we redo the TD without the corresponding r_{ij} .

C. Include GA

After TD, it is still required to do GA in order to have the actual real world coordinates. But because the resulting topology from NLS will slightly differ from the true topology, the GA by translating and rotating the topology to match measured world positions of some anchors is likely infeasible, and could even result in a large calibration error. It is better to include the GA directly in the NLS, adding the weighted squared errors of the few measured anchor world positions $x_{k,\text{meas}}$, with a much lower spread σ_{GA} , to the NLS. The NLS cost function (14) now changes

into

$$\sum_{ij} \left(\frac{r_{ij} - \|\hat{x}_i - \hat{x}_j\|}{\sigma_{\text{UWB}}} \right)^2 + \sum_k \left(\frac{\|\hat{x}_k - x_{k,\text{meas}}\|}{\sigma_{\text{GA}}} \right)^2. \quad (16)$$

Note that indices i, j , and k only iterate over those devices, for which UWB ranges or anchor positions are available. The advantage of including GA is that the topology is immediately corrected by the measured anchor positions. In fact, doing so yields the true posterior covariance matrix of all device positions *given all available measurements*, which are both the UWB ranges and the manually measured anchor positions.

D. Tag Localization

The estimated anchor positions \hat{a}_i might still differ from the true positions a_i . These errors $\hat{a}_i - a_i$ will distort a subsequent tag localization \hat{t} . Therefore, we apply the same principle as before, reformulating the tag localization as the MLE of all device positions given all UWB ranges, including those used during autocalibration. But all autocalibration information is already (approximately) captured by the estimate \hat{a} with covariance matrix $\text{Cov}[\hat{a} - a]$. Because the UWB ranges r_i between the anchors and the new tag are now added, we not only estimate the tag position \hat{t} , but also update the anchor positions estimate \hat{a}' . The NLS cost function is now

$$\sum_i \left(\frac{r_i - \|\hat{a}'_i - \hat{t}\|}{\sigma_{\text{UWB}}} \right)^2 + (\hat{a}' - \hat{a})^T \text{Cov}[\hat{a} - a]^{-1} (\hat{a}' - \hat{a}) \quad (17)$$

which is minimized over \hat{t} and \hat{a}' , given r_i , \hat{a} and $\text{Cov}[\hat{a} - a]$. Again, anchor indices i only iterate over those anchors "visible" for the tag by UWB, but the second NLS term covers all anchors. This formulation has the advantage of flexibility of the anchor positions estimate, such that errors in \hat{a} less distort the tag localization. Yet, for stability reasons, we do not update the anchor position estimate \hat{a} for future tag localizations.

E. Tag Localization Uncertainty

As mentioned in Section III-B, one can evaluate the autocalibration by the uncertainty $\text{Cov}[\hat{a} - a]$ of the anchor positions estimate \hat{a} . It is however more useful to evaluate the *resulting* tag localization uncertainty $\text{Cov}[\hat{t} - t]$. This can again be calculated as the inverse Hessian of the NLS cost function for localization (17) and crop out the part corresponding to \hat{t} . However, such calculation is rather tedious, especially if we want to evaluate this for multiple tag positions to build an uncertainty heatmap. But we do not need to solve the NLS to evaluate the posterior estimate's covariance. Instead, we use the covariance update formula for recursive LS [27], and use the formula of inverted block matrix [28] to crop out the covariance of the tag localization

$$\begin{aligned} \text{Cov}[\hat{t} - t] = & \left(\sigma_{\text{UWB}}^{-2} J_r(t)^T J_r(t) - \sigma_{\text{UWB}}^{-2} J_r(t)^T J_r(a) \left(\text{Cov}[\hat{a} - a]^{-1} \right. \right. \\ & \left. \left. + \sigma_{\text{UWB}}^{-2} J_r(a)^T J_r(a) \right)^{-1} \sigma_{\text{UWB}}^{-2} J_r(a)^T J_r(t) \right)^{-1} \end{aligned} \quad (18)$$

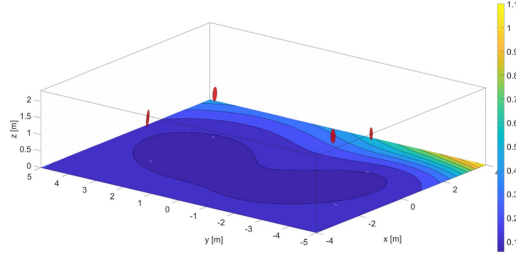


Fig. 8. Visualization of anchor position estimate and resulting localization uncertainty. The ellipsoids are the 3σ -blobs of the anchor positions. The heatmap shows the worst 2-D error (3σ) for each position.

with $J_r(a) \in \mathbb{R}^{m \times 3n}$ and $J_r(t) \in \mathbb{R}^{m \times 3}$ the Jacobian matrices of the A2T distances $[\|a_1 - t\|, \dots, \|a_m - t\|]^T$, to the anchor and tag coordinates a_i and t , respectively. Of the total of n anchors, there are m anchors for which there is an UWB range measurement to the tag. Note that we do not need the tag location estimate \hat{t} , by solving (17), to evaluate (18) for a grid of tag positions t . Instead, this can be done right after autocalibration, which is solving the NLS defined by (16).

To assess the autocalibration and resulting localization, we can plot the estimates \hat{a}_i with their uncertainty and the localization uncertainty $\text{Cov}[\hat{t} - t]$ together. An example with four anchors is shown in Fig. 8. We visualize the anchor uncertainties represented by $\text{Cov}[\hat{a} - a]$ by cropping out the 3×3 -block diagonal, which are the marginal covariance matrices $\text{Cov}[\hat{a}_i - a_i]$ of each anchor. These can be visualized as ellipsoids around the anchor position estimates, as shown in Fig. 8. The ellipsoids are the 3σ -blobs, whose principal axes' directions and sizes are calculated from the singular value decomposition of each block $\text{Cov}[\hat{a}_i - a_i]$. The heatmap visualizes the worst 2D-localization error for each position on the floor, set to $3\sigma_{\text{loc},2D}$, where $\sigma_{\text{loc},2D}$ is the highest singular value of the upperleft 2×2 part of $\text{Cov}[\hat{t} - t]$. In this 2D-scenario, we have left out the third dimension of $\text{Cov}[\hat{t} - t]$, only considering localization (and its uncertainty) in the xy -plane. In the particular example case of Fig. 8, it could be judged from the size of the ellipsoids that the anchor positions estimate uncertainty cannot be reduced much more. Therefore, if a higher localization accuracy is desired, one could consider placing an extra anchor. We note that there is a similarity between what is shown in the heatmap and geometric dilution of precision [29].

F. Experimental Demonstration of Combined Calibration

In this section, we present the results of an extensive outdoor experiment aimed at showcasing the viability of both device and system calibrations. As depicted in Fig. 9, the experimental setup involves a tag positioned on a controlled linear slide that spans 9 m. This tag's position was continuously monitored by a network of eight uniformly arranged UWB anchors. In addition, an external camera system was strategically deployed to record the tag's real-time location with an accuracy smaller than 1 cm, serving as our ground truth. A comparative analysis was conducted between the coordinates obtained from the UWB system and those captured by the camera to assess the tag's localization accuracy within the specified setup.

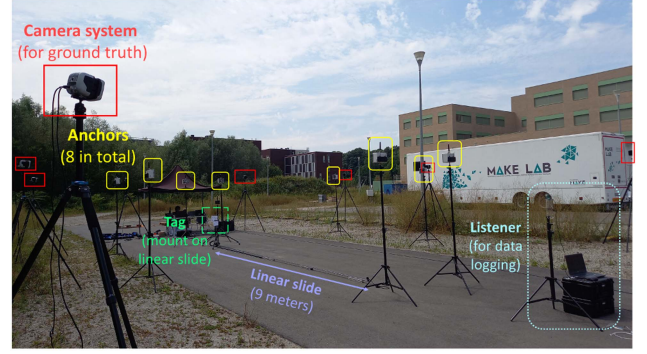


Fig. 9. Outdoor calibration setup: red boxes are the camera system used for ground truth; yellow boxes are the eight UWB anchors; green box is the tag mounted on a 9-m linear slide; and the cyan box is the listener for data logging.

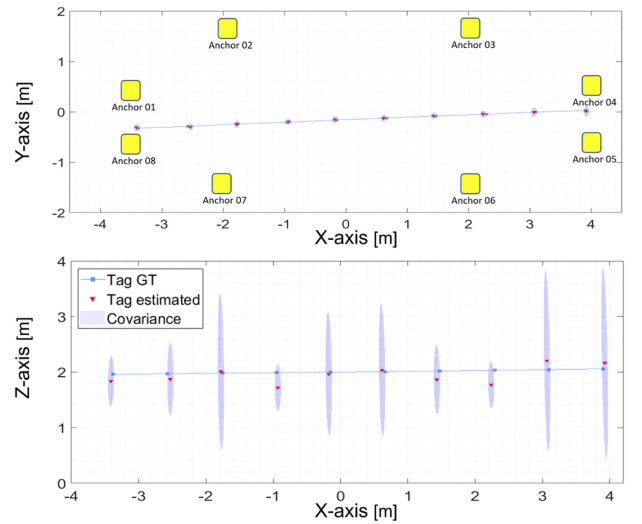


Fig. 10. Comparative analysis of the tag's estimated position against the ground truth. The close alignment in the x - y plane and x - z plane indicates robust positioning performance. The shaded regions represent the predicted uncertainty bounds, within which the actual position likely resides. It can also be observed that the 2-D uncertainty in x - y plane is in general very small for each point, while the vertical uncertainty is much bigger. This is because the anchors are positioned at spatially spread locations in x - y plane but not in the z -axis as they are at almost the same height.

For the experimental results, we first recorded A2A and A2T UWB ranging measurements, using device-calibrated hardware, for a few random positions of a single tag, and performed the system calibration procedure Steps 1–4. We collected data at ten distinct positions uniformly from the tag's linear trajectory and plot the ground truth with the estimated uncertainty in Fig. 10. For the X - Y plane, the estimated position closely aligns with the ground truth, with the latter consistently falling within the uncertainty region. This indicates a robust system performance in the horizontal plane. For the X - Z plane, the estimated position is still quite close to the ground truth with a slightly more pronounced deviation. Nevertheless, the majority of the ground truth data still resides within the uncertainty bounds. Moreover, both the bias and uncertainty in the x - z plane are more substantial than in the x - y plane, and this is expected given that all the anchors

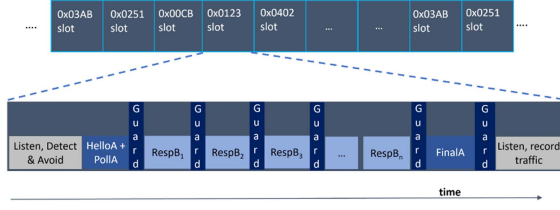


Fig. 11. Time-slot for each TALKER in AURA protocol. Strings like “0x03AB”, “0x0251” refer to the IDs of different devices.

were positioned at the same height, leaving more uncertainty on the Z-axis.

It is worth noting that this experiment primarily aims to demonstrate the qualitative added value of this method rather than a definitive accuracy validation, as real-world accuracy much depends on the specific configuration of the application. The benefits of this system calibration method are on the one hand the facilitation of a statistically sound anomaly detection as the method’s output includes the posterior distribution of anchor and tag positions given all available information. It also provides insight in the achievable accuracy for the envisioned localization application. On the other hand, the method offers a significant reduction in effort required for anchor calibration, as only a few anchors need manual position measurements.

IV. AUTOMATIC UWB RANGING ANY-TO-ANY (AURA)

As outlined in Section III-A, with the increasing complexity of UWB systems, there is a clear need for advanced protocols to ensure smooth device communication and avoid potential conflicts. In this section, we introduce a protocol named AURA, designed to ensure automatic ranging between any UWB devices and accurate network topology formation.

A. AURA Protocol

The AURA protocol streamlines UWB communication roles into two fundamental entities: the LISTENER and the TALKER. Listeners solely listening UWB messages, whereas talkers engage in TWR with each other. While not transmitting, each talker acts as a listener, observing who transmits messages. They respond to TWR requests in a specific sequence when prompted by the initiator (act as responder), and will eventually become to the initiator at some point.

In other words, a talker’s operation within AURA encompasses two modes: passive listening and active transmitting. In the passive mode, talkers observe ongoing transmissions, noting other TWR messages and which other talkers IDs are active in the vicinity, and get ready to answer in a set sequence if called upon. During active mode, they alternate in assuming the role of the initiator. This alternating role is governed by scheduled time slots, during which each talker has an opportunity to act as the initiator. Each time slot has a fixed timetable that sets the order to follow when an initiator is communicating with multiple responders, as shown in Fig. 11.

One of the key features of AURA protocol is its channel-awareness. Before initiating communication, the chosen initiator

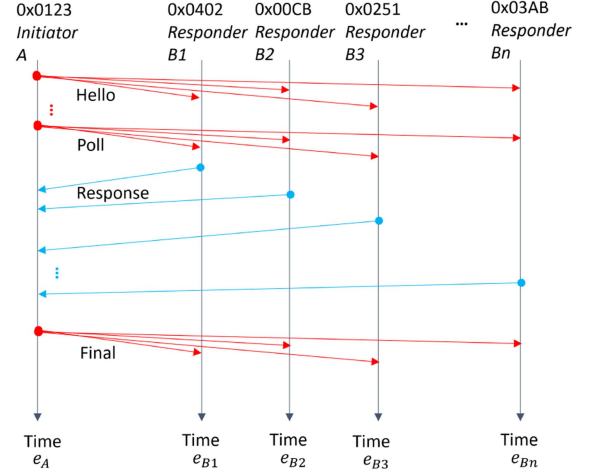


Fig. 12. TWR between TALKERS in AURA protocol. Each arrow represents the UWB message sent by each TALKER. Red arrows represents messages sent from the initiator while blue arrows indicate messages from the responders. Since the device is listening to traffic when not transmitting, other TWR messages are also recorded and at the same time it synchronizes the TWR schedule with other devices.

employs a “detect and avoid” mechanism. If the channel is occupied, the initiator delays its transmission by a time slot extended with a small random interval, ensuring collisions are avoided. Once a clear channel is found, the initiator sends out the “Hello and Poll” messages, which include the IDs of anticipated responders and their response sequence. The devices that need to respond are then send the “Response” message according to the order specified in the “Hello and Poll” messages from initiator. Within an initiator’s designated time slot, there is time allocated for a fixed number of responders to respond. Once this time is passed, the initiator wraps up the TWR with a “Final” message. Subsequently, a different device takes over as the initiator, beginning its TWR session. The whole procedure is illustrated in Fig. 12.

To better understand AURA’s functioning, picture the dynamics of a structured conference meeting. In such settings, there might be a predefined schedule of speaking turns. However, participants are often flexible and patient. If a speaker goes beyond their allocated time or starts early, others wait, maintaining the flow of the discussion. Without such an implicit protocol, discussions could quickly become chaotic, leading to overlapping conversations and missed information.

Similarly, AURA ensures a structured exchange of information, with each device, much like a conference participant, understanding its turn to send or receive data. This is especially critical in scenarios requiring automatic topology determination, where devices need to identify and establish their relative positions on their own. With AURA, not only is auto-TD possible, but the overall communication is more streamlined, systematic, and adaptable to different situations. This paves the way for numerous novel UWB applications.

Another key feature of AURA protocol is continuous relative clock calibration, by using initiator’s clock as reference clock in each TWR time slot. Each device that receives the “Hello and Poll” messages can immediately calculate its relative clock

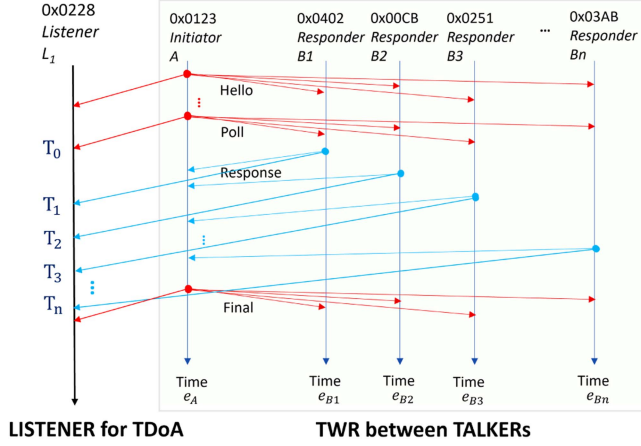


Fig. 13. Downlink-TDoA application: A listener device captures timestamped messages from TALKERS during communication exchanges. As also explained in Fig. 12, each arrow represents the UWB message sent by each TALKER. Note that in this case there is no message sent by the LISTENER, it is just listening and captures all the messages. The shaded area represents the general TWR process within the AURA protocol, as depicted in Fig. 12. The unshaded area indicates an additional LISTENER device intercepts the TWR messages for its own use. The LISTENER first corrects the timestamps with relative clock calibration, then computes the corrected time differences of arrival. From these information and the known positions of the TALKERS, it can compute its own position.

offset to the initiator's clock using the relative clock calibration method described in Section II-A. The "Response" message from each responder also contains the computed relative clock offset to the initiator and the reply delay (delay from received "Poll" message to the transmit of "Response" message). By doing so, each device that listens these messages can perform corrections of the timestamps using initiator's clock as the reference clock. In other words, in each TWR time slot (from "Hello and Poll" until "Final" messages), every device can synchronize its own clock to initiator's clock.

B. Benefits and Applications of AURA

In this section we provide two distinguished use cases of AURA, emphasizing its proficiency in accurate location determination and its adaptability across dynamic contexts. Moreover, AURA can extend to accommodating various scenarios, as long as they rely on the ToA-based methodology for localization or tracking. This includes applications in Wi-Fi RTT and 5G positioning utilizing New Radio positioning reference signals (NR PRS), among others.

1) **Downlink TDoA:** The first compelling application of the AURA system is DL-TDoA. Traditionally, TDoA methodologies rely on discerning the time difference between the arrivals of multiple signals at a single device or across various clock-synchronized devices—a process often with difficult synchronization challenges. However, AURA offers a streamlined solution, enabling easy implementation of DL-TDoA for any listener device, as depicted in Fig. 13.

The methodology is as follows: initially, the listener monitors messages between initiator and responders. It first records the "Hello and Poll" messages to get the relative clock offset

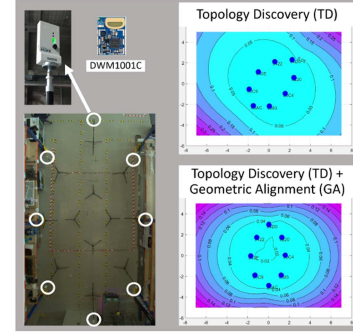


Fig. 14. Example use case: from TD to GA. Top left: MDEK1001 platform that is used as UWB beacon to perform the experiments. Bottom left: placement of beacons as seen from ceiling mounted camera. Top right: the result of TD. Bottom right: result after applying GA.

between itself and Initiator A. The "Poll" received timestamp T_0 is used as the starting time. Subsequent "Response" messages are also captured with their specific arrival timestamps: T_1 , T_2 , T_3 , and so on. Each "Response" message also contains the reply delay and the responder's relative clock offset to the initiator's clock. At the end, the initiator transmit the "Final" message that includes the computed ToF using SS-TWR to all the responders that responded within this TWR time slot. With these information, all the timestamps can be corrected and then the listener can calculate the TDoA for the received signals emitted by the responders. By comparing these TDoAs and knowing the positions of the responders, the listener can derive its position.

One of the main advantages of DL-TDoA is the unlimited amount of the mobile tags, since in this case the tags are just listeners. Another advantage of DL-TDoA is privacy, since the position computation is performed on the user side, the user has full control whether or not the resulting position can be shared.

2) **Simultaneous Localization and Calibration:** In this part we will present another compelling use case involving AURA with an experiment. Since AURA enables automatic ranging between beacons, combining it with the System Calibration described in Section III enables continuous TD, which is actually relative position between beacons to each other. In other words, this allows automatic anchors calibration and tags localization with uncertainty indications (serving as a guide for optimal anchor placement). It also adjusts in real-time when anchors are moved. The data for this verification experiment is derived from real UWB ranging data.

For our hardware setup, we utilize the MDEK1001 board, which is built upon the DWM1001C module from Qorvo. We then implemented our firmware that includes the AURA protocol on these modules. We start with placing the beacons into a configuration depicted in Fig. 14 (bottom left). As the beacons engage in ranging per the AURA protocol, the collected range measurements leads to an initial topology, as seen in the top right of Fig. 14, i.e., the TD procedure. Subsequently, a GA is executed to align this relative topology with an actual-world frame, depicted at the bottom right of Fig. 14.

It is important to note that the TD computation is not static. Once the GA is complete, the protocol ensures the system can monitor beacon movements and tracks changes in real-time. The

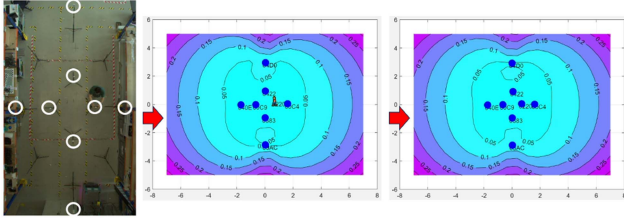


Fig. 15. SLAC. Left: geometry of the moved setup as seen from ceiling mounted camera. Middle: the transitional state in which the system indicates the moving beacons (shown as a human icon in the graph) and strives to discover the topology. Right: final discovered topology after the moving beacons are not moving anymore. The heatmap shows the 2-D error (3σ) for each position.

beacons that are currently not moving take the role of anchors, until they move. When we move some beacons as shown in the ceiling mounted camera image, left panel of Fig. 15, the system automatically detects this and makes sure the fixed beacons keep their previous world coordinates. In our observations, as long as a sufficient number of spatially distributed beacons remain stationary at the same time, the world frame, initially set after GA, is consistent in time. This minimum number of stationary beacons varies based on the environmental and topological complexities, but the absolute minimum is three.

The possibilities of this SLAC system are vast and varied. Consider a giant warehouse or large-scale industries where the layout needs frequent alterations to optimize space or accommodate new inventory. Traditional systems would require a cumbersome recalibration each time anchors are moved. With SLAC, these adjustments become seamless. In addition, in ever-changing environments, such as exhibition centers or convention halls, SLAC ensures that localization systems can be quickly adapted to new configurations.

V. CONCLUSION

In this study, we successfully demonstrated the determination and mitigation of systematic errors in UWB localization, effectively tackling challenges at both device and system levels. Our methodology encompasses precise bias measurement and calculation, addressing CFO and drift, and is adaptable for scenarios with or without an absolute reference clock. Furthermore, we established a straightforward yet effective relationship between RSSI and bias, alongside developing a dependable method for ascertaining device-specific hardware delay. Our work also includes the introduction of an anchor calibration method that significantly reduces the reliance on manual position measurements. Utilizing redundancy, we laid a statistical groundwork for the detection and elimination of outliers, thereby facilitating a critical assessment of the ensuing localization accuracy. A pivotal aspect of our research is the development of the AURA protocol, which significantly augments the flexibility of UWB localization. This protocol is versatile, applicable to a range of scenarios including downlink TDoA and SLAC, and is designed to adapt to changing conditions, thereby continually optimizing localization accuracy. Our findings, corroborated with real UWB data, not only underscore the efficacy of our methods in UWB

technology but also highlight their potential applicability to analogous technologies, such as WiFi RTT and 5G NR PRS, leveraging the common principle of using signal timestamps for ranging and localization.

REFERENCES

- [1] T. K. Geok et al., "Review of indoor positioning: Radio wave technology," *Appl. Sci.*, vol. 11, no. 1, pp. 279, 2020.
- [2] P. S. Farahsari, A. Farahzadi, J. Rezazadeh, and A. Bagheri, "A survey on indoor positioning systems for IoT-based applications," *IEEE Internet Things J.*, vol. 9, no. 10, pp. 7680–7699, May 2022.
- [3] Z. Liu, A. Zhang, and W. Wang, "A framework for an indoor safety management system based on digital twin," *Sensors*, vol. 20, no. 20, 2020, Art. no. 5771.
- [4] M. Elsanhoury et al., "Precision positioning for smart logistics using ultra-wideband technology-based indoor navigation: A review," *IEEE Access*, vol. 10, pp. 44413–44445, 2022.
- [5] F. Zafari, A. Gkelias, and K. K. Leung, "A survey of indoor localization systems and technologies," *IEEE Commun. Surv. Tut.*, vol. 21, no. 3, pp. 2568–2599, Jul.–Sep. 2019.
- [6] A. Poullose, J. Kim, and D. S. Han, "A sensor fusion framework for indoor localization using smartphone sensors and Wi-Fi RSSI measurements," *Appl. Sci.*, vol. 9, no. 20, 2019, Art. no. 4379.
- [7] G. Ouyang and K. Abed-Meraim, "A survey of magnetic-field-based indoor localization," *Electronics*, vol. 11, no. 6, 2022, Art. no. 864.
- [8] C. Li, L. Mo, and D. Zhang, "Review on UHF RFID localization methods," *IEEE J. Radio Freq. Identif.*, vol. 3, no. 4, pp. 205–215, Dec. 2019.
- [9] W. Guan, S. Chen, S. Wen, Z. Tan, H. Song, and W. Hou, "High-accuracy robot indoor localization scheme based on robot operating system using visible light positioning," *IEEE Photon. J.*, vol. 12, no. 2, Apr. 2020, Art. no. 7901716.
- [10] A. Ghosh, A. Maeder, M. Baker, and D. Chandramouli, "5G evolution: A view on 5G cellular technology beyond 3GPP release 15," *IEEE Access*, vol. 7, pp. 127639–127651, 2019.
- [11] J. A. Del Peral-Rosado et al., "Whitepaper on new localization methods for 5G wireless systems and the Internet-of-Things," in *Proc. White Paper COST Action CA15104 IRACON*, 2018, pp. 1–27.
- [12] L. Barbieri, M. Brambilla, A. Trabattini, S. Mervic, and M. Nicoli, "UWB localization in a smart factory: Augmentation methods and experimental assessment," *IEEE Trans. Instrum. Meas.*, vol. 70, 2021, Art. no. 2508218.
- [13] N. Dwek et al., "Improving the accuracy and robustness of ultra-wideband localization through sensor fusion and outlier detection," *IEEE Robot. Autom. Lett.*, vol. 5, no. 1, pp. 32–39, Jan. 2020.
- [14] A. Poullose and D. S. Han, "UWB indoor localization using deep learning LSTM networks," *Appl. Sci.*, vol. 10, no. 18, 2020, Art. no. 6290.
- [15] A. Poullose and D. S. Han, "Feature-based deep LSTM network for indoor localization using UWB measurements," in *Proc. Int. Conf. Artif. Intell. Inf. Commun.*, 2021, pp. 298–301.
- [16] J. Sidorenko, V. Schatz, N. Scherer-Negenborn, M. Arens, and U. Hugentobler, "Error corrections for ultrawideband ranging," *IEEE Trans. Instrum. Meas.*, vol. 69, no. 11, pp. 9037–9047, Nov. 2020.
- [17] A. R. Jiménez Ruiz and F. Seco Granja, "Comparing Ubisense, BeSpooon, and decawave UWB location systems: Indoor performance analysis," *IEEE Trans. Instrum. Meas.*, vol. 66, no. 8, pp. 2106–2117, Aug. 2017.
- [18] D. Neiryneck, E. Luk, and M. McLaughlin, "An alternative double-sided two-way ranging method," in *Proc. 13th Workshop Positioning Navigation Commun.*, 2016, pp. 1–4.
- [19] J. Cano, G. Pagès, E. Chaumette, and J. LeNy, "Clock and power-induced bias correction for UWB time-of-flight measurements," *IEEE Robot. Autom. Lett.*, vol. 7, no. 2, pp. 2431–2438, Apr. 2022.
- [20] J. Cheng, K. Guan, and F. Quitin, "Direction-of-arrival estimation with virtual antenna array: Observability analysis, local oscillator frequency offset compensation, and experimental results," *IEEE Trans. Instrum. Meas.*, vol. 70, Jun. 2021, Art. no. 5503113, doi: 10.1109/TIM.2021.3088434.
- [21] X. Gui, S. Guo, Q. Chen, and L. Han, "A new calibration method of UWB antenna delay based on the ADS-TWR," in *Proc. 37th Chin. Control Conf.*, 2018, pp. 7364–7369.
- [22] C. L. Sang, M. T. Adams, M. Hörmann, M. Hesse Porrmann, and U. Rückert, "Numerical and experimental evaluation of error estimation for two-way ranging methods," *Sensors*, vol. 19, no. 3, 2019, Art. no. 616.
- [23] DECAWAVE APS011 APPLICATION NOTE: Sources of error in DW1000 based two-way ranging (TWR) Schemes, Version 1.0, p. 10. [Online]. Available: <https://www.decawave.com>

- [24] DECAWAVE DW 1000 User Manual, Version 2.15, p. 45. [Online]. Available: <https://www.decawave.com>
- [25] C. Dym, *Principles of Mathematical Modeling*. Amsterdam, The Netherlands: Elsevier, 2004.
- [26] R. E. Kass, L. Tierney, and J. B. Kadane, "Laplace's method in Bayesian analysis," *Contemporary Math.*, vol. 115, pp. 89–99, 1991.
- [27] H. Monson Hayes, *Statistical Digital Signal Processing and Modeling*. Hoboken, NJ, USA: Wiley, 1996.
- [28] Dennis S. Bernstein, "Matrix Mathematics," in *Matrix Mathematics*. Princeton, NJ, USA: Princeton Univ. Press, 2009.
- [29] Richard B. Langley et al., "Dilution of precision," *GPS World*, vol. 10, no. 5, pp. 52–59, 1999.



Risang Yudanto received the graduation degree in telecommunication engineering from the Bandung Institute of Technology, Bandung, Indonesia, in 2003, and the master's and Ph.D. degrees in satellite navigation from the Electronic Department, Politecnico di Torino, Turin, Italy, in 2006 and 2010, respectively.

In 2011, he joined Flanders Make, Leuven, Belgium, where he is currently working as Senior Application Engineer. His research interests include wireless indoor positioning

systems, sensor fusion, radar system, sensors signal processing, and computer vision.



Jianqiao Cheng received the B.E. degree in electrical and electronics engineering from Beijing Jiaotong University, Beijing, China, in 2016, the M.Sc. degree in electrical engineering and computer science from the Queen Mary University of London, London U.K., in 2017, and the Ph.D. degree in electrical engineering with the Embedded Electronics research unit, Université libre de Bruxelles, Brussels, Belgium, in 2021.

He has been a Researcher with Flanders Make, Leuven, Belgium, since 2023. His research interests include wireless communication, unmanned aerial vehicle, indoor positioning, SLAM, autonomous robotics, and computer vision.



Erik Hostens received a master degree magna cum laude in electromechanical engineering, and a Ph.D. degree in quantum information theory from KU Leuven, Leuven, Belgium, in 2003 and 2007, respectively.

He has industrial experience in advanced process control (RandD, Siemens). Since 2010, he has been employed with Flanders Make, Leuven, and currently works as a Senior Researcher and Project Leader in the areas of his research interests which include systems and

control, estimation, optimization, and machine learning.



Miel Van der Wilt received the B.Sc. and M.Sc. degrees in mechanical engineering from KU Leuven, Leuven, Belgium, in 2017 and 2020, respectively.

He has been working as a Research Engineer with Flanders Make, Leuven, since 2021 in the areas of his research interests which includes indoor localization and control engineering.



Mats Vande Cavey received the M.Sc. degree in energy engineering from KU Leuven, Leuven, Belgium, in 2012.

After completing the M.Sc. degree, he joined the Applied Mechanics and Energy Conversion division, where he worked on model predictive control for energy management in buildings. Since 2016, he has been a Research Engineer with the Motions Core Lab, Flanders Make, Leuven, working on the areas of data processing, machine learning and data visualization for

building automated control algorithms and decision support in the manufacturing industry.